RESEARCH ARTICLE

Calibration-free parallel transmission of the cervical, thoracic, and lumbar spinal cord at 7T

Christoph S. Aigner[1] | Manuel F. Sánchez Alarcon[1,2] | Alexandre D'Astous[3,4] | Eva Alonso-Ortiz[5,6] | Julien Cohen-Adad[5,6,7,8] | Sebastian Schmitter[1,7,8]

Correspondence
Christoph S. Aigner, Department of Biomedical Magnetic Resonance, Physikalisch-Technische Bundesanstalt (PTB), Abbestr. 2-12, 10587 Berlin, Germany.
Email: christoph.aigner@ptb.de

Abstract

Purpose: To address the limitations of spinal cord imaging at ultra-high field (UHF) due to time-consuming parallel transmit (pTx) adjustments. This study introduces calibration-free offline computed universal shim modes that can be applied seamlessly for different pTx RF coils and spinal cord target regions, substantially enhancing spinal cord imaging efficiency at UHF.

Methods: A library of channel-wise relative B_1^+ maps for the cervical spinal cord (six datasets) and thoracic and lumbar spinal cord (nine datasets) was constructed to optimize transmit homogeneity and efficiency for these regions. A tailored B_0 shim was optimized for the cervical spine to enhance spatial magnetic field homogeneity further. The performance of the universal shims was validated using absolute saturation based B_1^+ mapping and high-resolution 2D and 3D multi-echo gradient-recalled echo (GRE) data to assess the image quality.

Results: The proposed universal shims demonstrated a 50% improvement in B_1^+ efficiency compared to the default (zero phase) shim mode. B_1^+ homogeneity was also improved by 20%. The optimized universal shims achieved performance comparable to subject-specific pTx adjustments, while eliminating the need for lengthy pTx calibration times, saving about 10 min per experiment.

Conclusion: The development of universal shims represents a significant advance by eliminating time-consuming subject-specific pTx adjustments. This approach is expected to make UHF spinal cord imaging more accessible and user-friendly, particularly for non-pTx experts.

KEYWORDS
7 Tesla, calibration-free, parallel transmission, spinal cord, universal pulse

1 | INTRODUCTION

Ultra-high field MRI (UHF; $\geq$ 7T) has revolutionized the field of human neuroimaging, offering unprecedented spatial resolution and contrast compared to MRI scanners operating at lower field strengths.[1] This technological advancement has been transformative in the study of the central nervous system (CNS), particularly for non-invasive diagnosis and longitudinal monitoring of neurological disorders such as multiple sclerosis (MS)[2,3] and amyotrophic lateral sclerosis (ALS).[4] For instance, early studies utilizing 7T MRI in the brain have demonstrated its ability to visualize more lesions and provide enhanced delineation of MS lesions, including the identification of the central vein sign, which was previously undetectable with conventional imaging modalities. The increased contrast and spatial resolution afforded by 7T MRI have also enabled the detection of subtler changes in MS pathology, allowing for a better characterization of lesion formation, cortical damage, and inflammation within the meninges.[5]

In recent years, the focus of 7T MRI research has been extended toward the spinal cord (SC), recognizing its involvement in a wide range of neurological disorders.[6] One of the primary challenges associated with 7T MRI in the SC is its anatomy (the SC measures approximately 450 mm in length and has a thin structure of nervous tissue ranging from 6 to 12 mm thickness) and its position within the vertebral column, necessitating high spatial resolution and large FOVs. Unfortunately, the short wavelength of the B_1^+ transmit field used at 7T causes spatially varying signal loss and compromised image quality in such images.

Despite these challenges, cervical SC imaging at UHF has been successfully demonstrated at exceptionally high spatial resolutions of 0.3 mm in-plane (while such sub-millimeter resolutions at 3T tend to be SNR limited)[6] with 2D multi-echo gradient-recalled echo (GRE),[7,8] T_1/T_2 weighted turbo spin-echo (TSE),[7] functional MRI (fMRI),[9] DWI,[10] or CEST[11] at 7T and 2D multi-echo GRE at 9.4T.[12] While promising preliminary studies have been conducted at 7T MRI in the thoracic and lumbar SC, for example,[13,14] systematic investigations remain limited due to the required FOV, lack of dedicated RF coils, and a stronger impact of the inhomogeneous B_1^+ transmit field due to the larger body dimensions in lower SC regions, as compared to the upper SC regions.[6]

The most flexible way to address the inhomogeneous B_1^+ transmit field is through tailored RF pulse design in combination with parallel transmission (pTx), a technique exploiting the spatial differences in the complex B_1^+ fields of the individual Tx channels of a multichannel pTx RF coil.[15] Although pTx was proposed more than 20 years ago, a fundamental challenge of pTx in the human body is its complex and time-consuming workflow that requires trained MRI operators, hampering the wider use and, therefore, the general progress of UHF MRI.[15]

The challenge of optimizing RF pulses for individual subjects has been effectively addressed by pre-computed dynamic universal pTx pulses (UP) in the human brain.[16] UPs are generated by optimizing across a library of B_1^+ maps from multiple subjects and can be applied to novel subjects without additional calibration, eliminating the need for time-consuming calibration procedures. Their effectiveness has inspired adaptations in other areas, such as the development of universal RF shims for spectroscopy in the head,[17] brain and C-spine,[18] or dynamic UPs in the heart[19,20] and C-spine.[21] Other calibration-free approaches have been proposed for brain imaging, including machine-learned slice-by-slice RF shims at 7T[22] and dynamic SmartPulses for liver imaging at 3T[23] or the combination of universal and tailored pulses for the brain at 7T.[24,25]

However, dynamic pTx is more sensitive to ΔB_0 variations and often exhibits lower temporal B_1^+ efficiency compared to static pTx (RF shimming) due to the use of gradients to traverse through excitation k-space.[15,26,27] These challenges are particularly pronounced in SC imaging due to the lower B_1^+ efficiency of SC coils compared to brain coils. Moreover, the curved SC anatomy makes it challenging to effectively compensate for ΔB_0 variations using vendor-provided tailored ΔB_0 shimming tools that are typically limited to cuboids. An alternative is the use of external custom ΔB_0 shimming tools[28] which offer more flexibility, but come at the cost of increased adjustment times. Otherwise, the measured ΔB_0 variations can be incorporated into the pTx pulse design[15] or prospectively compensated for using broadband pTx RF pulses.[26]

In this in-vivo study, we investigate the feasibility and benefits of using universal RF shims (US) to optimize the B_1^+ transmit and B_1^+ efficiency profiles in the cervical, thoracic, and lumbar spine. The US solutions are successfully validated at 7T in three previously unexamined subjects, covering the cervical and the thoracic/lumbar SC, respectively.

2 | METHODS

2.1 | MR scanner hardware

MRI Scans were conducted on a 7T scanner (Magnetom 7T, Siemens Healthineers, Erlangen, Germany) using pTx (step 2.3) using two commercial RF coils in two separate experiments for the C-spine and TL-spine regions, respectively. The first coil (MRI.Tools GmbH, Germany) was tailored for neck imaging and consists of an eight-channel

posterior-only transmit/receive array used to image the C-spine. The second coil (MRI.Tools GmbH, Germany) was tailored for body imaging and consists of two segments, an anterior and a posterior segment, with 32 elements which were employed as an 8-channel transmit and 32-channel receive array used to image the TL-spine. Both coils were certified to comply with IEC 60601-1 and IEC 60601-2-33 standards and approved for human use by the local ethics board. Local specific absorption rate (SAR) limits were incorporated by limiting the RF power of each transmit channel as described in more detail in previous works.[27,29] MRI data reconstruction, manual selection of SC ROIs, RF pulse design, tailored ΔB_0 shimming, and pulse file creation were performed offline on a workstation equipped with 12 cores, 2.1 GHz clock speed and 128 GB RAM. Besides tailored ΔB_0 shimming, which was performed in Python, all other tasks were performed in MATLAB (The MathWorks, Natick, MA).

2.2 | Subject information

MRI scans were performed on healthy subjects following approval from an Institutional Review Board and written informed consent. In total, 21 subjects (9 males and 12 females, aged 21–56 y, with body mass indexes (BMIs) ranging from 18 to 35 kg/m^2) were scanned in three different groups to create two library and an unseen test case group. In the first library group (libCSpine), six different subjects (four male and two female, 28–34 y, 18–27 kg/m^2) underwent MRI scans of the cervical spine to generate a B_1^+ library for offline tailored and universal shim (US) design. In the second library group (libTLSpine), nine different subjects (four male and five female, 26–56 y, 20–35 kg/m^2) underwent MRI scans of the torso to generate a B_1^+ library for offline tailored and US design in the thoracolumbar

spine. The third group (testCTLSpine) included three previously unseen subjects (one male and two female, 27–32 y, 21 to 26 kg/m^2) to test the two USs. These three subjects underwent the same scan protocol as libCSpine and libTL-Spine, with additional scans using the pre-calculated USs. Tables 1 and 2 give an overview of all relevant sequence parameters of this study.

2.3 | Subject positioning

At the start of each scan, the subjects were positioned in a standardized manner within the two RF coils. The neck coil comprises an anatomically fitted coil housing with a head casing that stabilizes the subject's position in the coil. After placing the subject in the neck coil, the isocenter was set 5 cm above the chin in head direction. The body array allows for more freedom when positioning the subject. The posterior half of the coil was centered at the subject's heart along the head-foot axis, while the anterior half was adjusted based on anatomical landmarks, maintaining a 2 cm gap between the coil and the subject's chin. The isocenter was set at a distance of 5 cm from the anterior coil center in head direction. All subjects were instructed to breathe normally and hold their breath in the inhale position (which is more convenient and results in less artifacts due to incomplete breath-holds based on our experience) when instructed via the intercom.

2.4 | ΔB_0 mapping and adjustment

Subject-specific ΔB_0 mapping and shimming was performed for the C-spine region using a 2D GRE sequence with the following parameters: nominal FA = 20°, TE1/TE2/TR = 3.06/4.08/818 ms,

TABLE 1 Sequence parameters of different B_1^+ mapping approaches.

Parameter	Relative 3D	Relative 2D	Absolute 2D
TR (ms)	5	4	5000
TE (ms)	2.02	1.78	2.18
TA (s)	205	5	10
Nominal FA (°)	20	15	8
Reference voltage (V)	170	170	170
FOV (mm^3)	250 × 312 × 312	384 × 224	384 × 384
Voxelsize (mm^3)	4 × 4 × 4	2 × 2 × 4	4.7 × 4.7 × 5
Bandwidth (kHz)	399	704	490
Spokes	256	-	-
Target anatomy	TL-spine	C-spine	C- and TL-spine

TABLE 2 Sequence parameters of B_0 mapping and Universal Shim (US) validation.

Parameter	2D GRE B_0 mapping	2D GRE US validation	3D GRE US validation
TR (ms)	818	40	27.69
TE (MS)	3.06/4.08	2.25/5.25/ … /14.25	2.04/4.08/6.12
TA (S)	213	10	204
Nominal FA (°)	20	30	10
Reference voltage (V)	170	170	170
FOV (mm³)	$256 \times 256 \times 256$	384×244	$352 \times 212 \times 192$
Voxelsize (mm³)	$2 \times 2 \times 2$	$1 \times 1 \times 2$	$1 \times 1 \times 1$
Bandwidth (kHz)	601	620/620/ … /620	646/646/646
Target anatomy	C-spine	TL-spine	C-spine

$FOV = 256 \times 256 \times 256\,mm^3$, voxel size of $2 \times 2 \times 2\,mm^3$, and $TA = 3\,min\,33\,s$. To enable ΔB_0 mapping we have exported the DICOM images to the above-mentioned workstation which was connected to the MR console via ethernet and that runs the *Shimming-Toolbox*.[28] The regularization-based ΔB_0 shimming process (using a regularization parameter of 0.001) involved a series of pre-processing steps: phase unwrapping using the scikit-image software with a threshold of 0.05 to eliminate phase ambiguity ($<10\,s$), manual identification of the SC centerline ($\sim1\,min$) and, automated cylindrical mask generation encompassing a region of interest (ROI) ($d = 20\,mm$) around the SC centerline ($<10\,s$). The last two steps were performed with the *Spinal Cord Toolbox*.[30] In total, tailored ΔB_0 shimming up to the 2nd order could be accomplished for the 3D C-spine volume in approximately 5 min for each of the three subjects. Substantial respiratory motion artifacts in the 2D GRE data covering the TL-spine region prevented subject-specific ΔB_0 mapping and shimming for the TL-spine region.

2.5 | B_1^+ mapping and adjustment

Relative and absolute B_1^+ maps for pTx calculations were acquired differently for the C-spine and TL-spine under free-breathing conditions. For C-spine, 2D relative B_1^+ maps were acquired using a Cartesian gradient-echo (GRE) sequence[31] (nominal $FA = 15°$, $TE/TR = 1.78/4\,ms$, $FOV = 384 \times 224\,mm^2$, voxel size $= 2 \times 2 \times 4\,mm^3$, $TA = 5\,s$). In TL-spine, 3D relative B_1^+ maps were obtained for each subject using a radial phase-encoding GRE scan (nominal $FA = 20°$, $TE/TR = 2.02/40\,ms$, $FOV = 250 \times 312 \times 312\,mm^3$, voxel $= 2 \times 2 \times 2\,mm^3$, $TA = 3\,min\,25\,s$).[29] After acquisition, the non-Cartesian raw data were exported to a remote workstation for reconstruction during the next MR scan, which took

approximately 2 min. The reconstructed, non-Cartesian B_1^+ maps had an isotropic voxel size of 4 mm and exhibited no visible motion-induced artifacts. The sum of magnitudes of the B_1^+ maps was employed to manually draw a (ROI) encompassing the SC, using the 2D B_1^+ maps to cover the vertebrae levels C1-C7 for C-spine and, in average across all subjects, three sagittal 2D slices out of the 3D B_1^+ maps to cover the vertebrae levels T1-L5 for TL-spine. It took less than 1 min to manually mark the ROIs in the sagittal orientation.[27] Please note that only the central sagittal 2D slice extracted from the 3D volume was used to design and evaluate the different RF shims. The ROIs were then utilized as a binary mask for tailored and calibration-free pTx US pulse design.

Tailored and universal phase-only RF shims (US) were optimized separately for the C- and for the TL-spine using a training library of six and nine subjects, respectively. This number is sufficient to cover inter-subject variations in SC curvature or thickness. A full analysis of USs with a different library size can be found in the Supporting Material. The RF shim design aimed to balance homogeneity using the coefficient of variation (CV):

$$CV = std\left(\left|\sum_{ch=1}^{N_c} B_{1,ch}^+(r)b_{ch}\right|_{ROI}\right) \Big/ mean\left(\left|\sum_{ch=1}^{N_c} B_{1,ch}^+(r)b_{ch}\right|_{ROI}\right)$$

and the mean of the transmit efficiency in the manual selected ROI ($mean(|\eta(r)|)_{ROI}$) using the spatial transmit efficiency $\eta(r)$:

$$\eta(r) = \left|\sum_{ch=1}^{N_c} B_{1,ch}^+(r)b_{ch}\right| \Big/ \sum_{ch=1}^{N_c} \left|B_{1,ch}^+(r)\right|$$

based on channel-wise B_1^+ maps at different spatial locations r in the library combined with one global set of

complex RF phase factors $b_{ch} = e^{i\Phi_{ch}}$ for manually selected SC ROIs. Note that the pulse design uses one scalar for homogeneity (CV) and efficiency ($\eta = \text{mean}(|\eta(r)|)_{ROI}$) whereas the later performed RF pulse evaluation uses a voxel-based analysis of the efficiency ($\eta(r)$) to assess the spatial distribution of the B_1^+ efficiency. To compute a US for multiple subjects, we aligned and stacked B_1^+ maps and SC ROIs from different subjects along the slice direction. Unlike dynamic pTx pulse design, where slice position influences the experienced gradient strength and stacking requires precise alignment of slice positions, static RF shimming eliminates the need for such intricate alignment and facilitates straightforward stacking, for example by setting $B_{1,ch}^+ = [B_{1,ch,1}^+, B_{1,ch,2}^+, \dots B_{1,ch,N_s}^+]$ and $\text{ROI} = [\text{ROI}_1, \text{ROI}_2, \dots \text{ROI}_{N_s}]$ with N_s being the number of subjects in the design library.

The above-described RF shim design aims to optimize two crucial parameters: the B_1^+ transmit homogeneity, quantified by the CV, and the B_1^+ transmit efficiency η. The CV quantifies the variation of B_1^+ across the ROI and η measures the efficiency of B_1^+ transmission. Ideally, we strive for a low CV (indicating a uniform field distribution) and a high η (indicating efficient RF usage). However, these parameters compete, and typically achieving a low CV comes at the expense of a lower η, and vice versa. Therefore, when designing a cost function used for optimization, these two terms are weighted based on which parameter is more critical for the specific application.

In this work, the utilized RF coils are B_1^+-limited. Consequently, we prioritize increasing the transmit efficiency and weight the cost function accordingly. Here, the weighting is 95% by η and 5% by CV. A full analysis of how different cost function weightings affect the results is presented in the results section. Due to the non-convex nature of the optimization process and to reduce the chance of ending up in an unfavorable local minimum, each optimization was performed eight times (this number was set empirically to avoid local minima) with different pseudo-random starting phases followed by an automated selection of the best solution based on the lowest cost function value. The computation times of the US were of the order of 1 min.

Figure 1 shows B_1^+ transmit and B_1^+ efficiency profiles of the C-spine and TL-spine at 7T using the default RF shim, the required steps to achieve the tailored RF shim[27] and the proposed calibration-free US for the first unseen subject of group testCTLSpine. The US for C-spine was computed using all six datasets of group libCSpine and the US for TL-spine was computed using all nine datasets of group libTLSpine. The code for the US design and the B_1^+ data sets can be downloaded from https://github.com/chaigner/UShim.

Three unseen test-cases (testCTLSpine) underwent additional, vendor-provided saturation based absolute B_1^+ mapping[32] with and without the US (nominal FA = 8°, TE/TR = 2.18/5000 ms, FOV = 384×384 mm^2, voxel size = $4,7 \times 4,7 \times 5$ mm^3, TA = 10 s) using a non-selective rectangular saturation pulse with an RF duration of 500 µs.

## 2.6 | Experimental validation of universal shims

3D high-resolution Cartesian multi-echo GRE scans were obtained for C-spine under free-breathing (nominal FA = 10°, TE1/TE2/TE3/TR = 2.04/4.08/6.12/27.69 ms, FOV = $352 \times 212 \times 192$ mm^3, voxel size = $1 \times 1 \times 1$ mm^3, TA = 3 min 24 s), and during breath-hold in 2D for TL-spine (nominal FA = 30°, TE1/TE2/ … /TE5/TR = 2.25/5.25/ … /14.25/40 ms, FOV = 384×244 mm^2, voxel = $1 \times 1 \times 2$ mm^3, TA = 10 s) in all three subjects of group testCTLSpine using the pre-computed US. In the case of TL-spine scans, the datasets were acquired with the tune-up ΔB_0 shim, whereas the datasets of the C-spine scans were acquired using the tailored ΔB_0 shim.

2.7 | Statistical analysis

A one-sample t-test was used to identify statistically significant differences in the CV and B_1^+ efficiency, η, of SC ROIs between different groups, for example, different RF shim settings or different subject groups. We performed the t-test with the null hypothesis that the difference of the CV or η from two groups comes from a normal distribution with a mean equal to 0 and unknown variance. The results were considered statistically significant if p was <0.05. Statistically significant results are denoted by a star (*) and non-statistically significant results are denoted by "NS" in the figures.

3 | RESULTS

Figure 1 provides a comprehensive overview of the influence of various RF shims on the resulting B_1^+ transmit and B_1^+ efficiency profiles for the first subject of the testCTLSpine group. It is noteworthy that the cost function for tailored and universal pulse design was designed to mainly improve the B_1^+ efficiency by weighting it with 95% for η (efficiency) and 5% for CV (homogeneity), which could be modified if necessary. A qualitative assessment reveals that both tailored and universal RF shims enhance the combined B_1^+ magnitude, homogeneity, and efficiency within
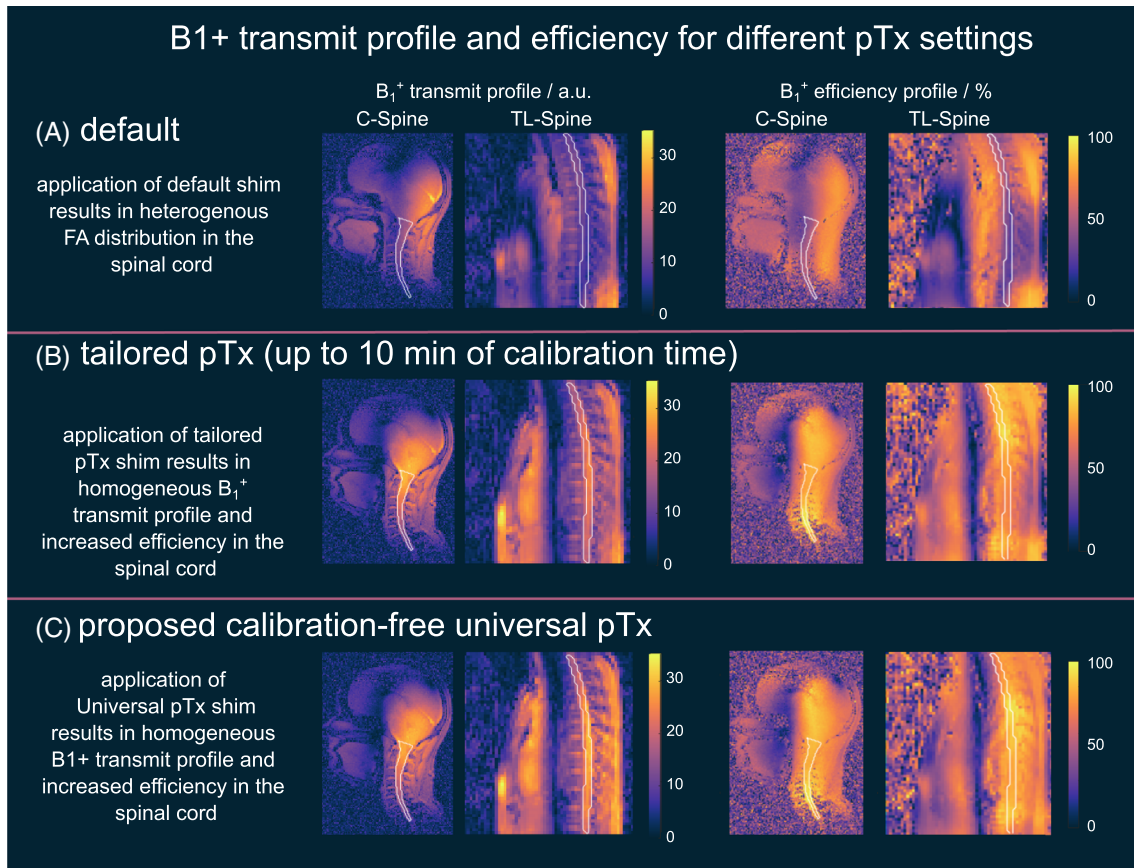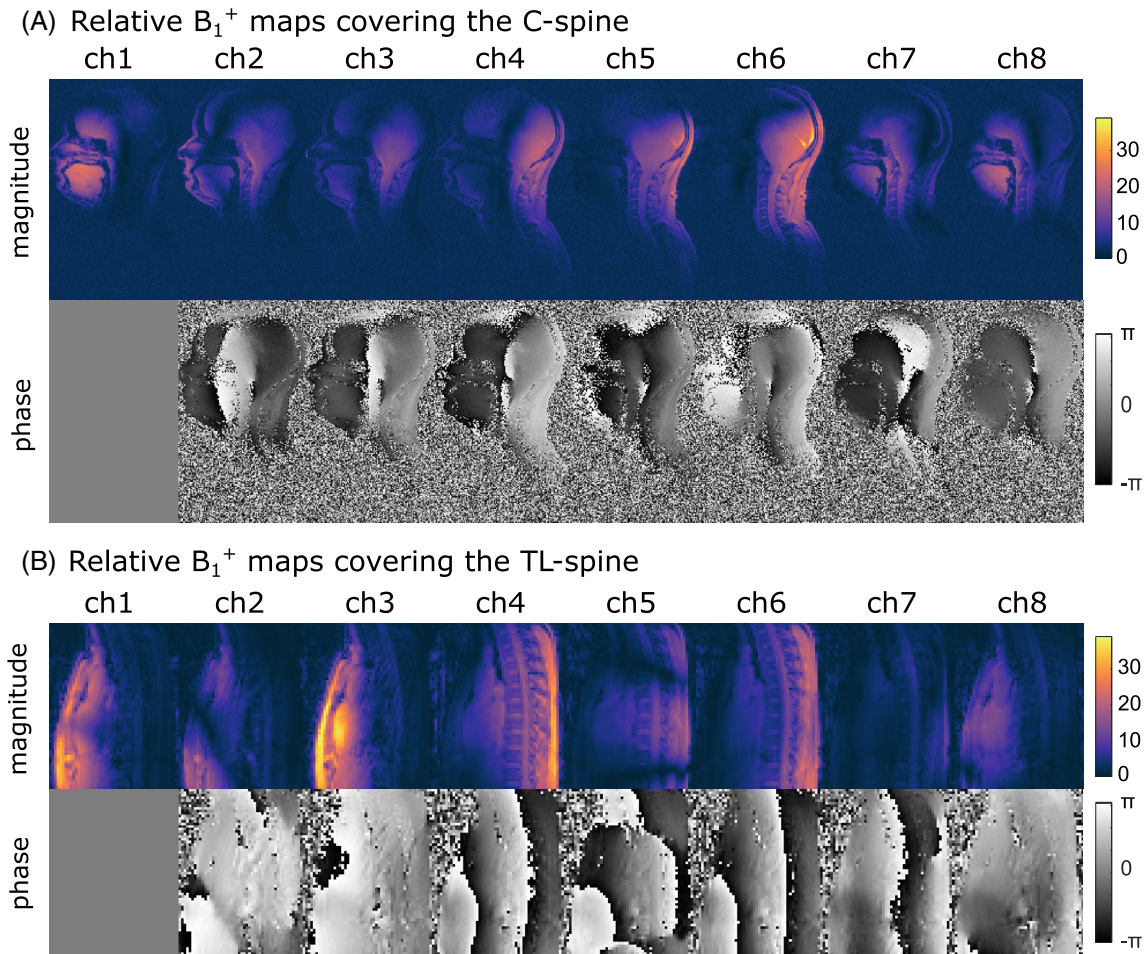
FIGURE 1 This figure illustrates the B_1^+ transmit and efficiency profiles predicted for three different pTx settings in the cervical spine and the thoracic and lumbar spine for the first subject of group testCTLSpine. (A) Default Shim: The application of the default shim (not optimized for the SC) results in a heterogeneous B_1^+ distribution and low B_1^+ efficiency in the SC, leading to suboptimal excitation quality. (B) Tailored pTx RF Shim: The tailored pTx RF shim, optimized specifically for the outlined ROI, demonstrates a significantly improved B_1^+ homogeneity and efficiency, translating into higher-quality SC images. (C) Universal pTx RF Shim: The precomputed calibration-free universal pTx RF shim, generated from a library of six and nine different B_1^+ datasets (C-spine and TL-spine), eliminates the need for lengthy pTx adjustments, saving up to 10 min of scan time.

the target region (delineated by a white overlay in the figure) compared to the default shim, which is not optimized for the C-spine or TL-spine. Quantitatively, for the C-spine, CV decreases from 31% (default) to 28% (tailored RF shim) and 27% (US), while the B_1^+ efficiency improves from 46% (default) to 91% (tailored RF shim) and 85% (US), which was the aim of the optimization. Similarly, for the TL-spine, the CV is reduced from 22% (default) to 12% (tailored RF shim) and 17% (US), and the B_1^+ efficiency increases from 40% (default) to 82% (tailored RF shim) and 82% (US). An efficiency increase of a factor of two corresponds to a two-fold higher FA, which would otherwise only be possible with four-fold RF power.

Figure 2 depicts the magnitude and phase of channel-wise relative 2D B_1^+ maps encompassing the C-spine (2 mm in-plane resolution; 4 mm slice thickness) and 3D B_1^+ maps including the TL-spine (4 mm isotropic) of the first subject from the unseen test cases of group testCTLSpine. Remarkably, both the magnitude

and phase of each of the eight channels do not reflect breathing artifacts, even in the torso where respiratory and cardiac motion is present, despite the underlying 3D Non-Cartesian GRE data being acquired under free-breathing conditions. This observation holds true for all subjects, demonstrating the robustness of our 3D Non-Cartesian GRE based relative B_1^+ mapping methodology in the presence of motion.

Figure 3 illustrates the trade-off between B_1^+ field homogeneity and transmit efficiency achieved by the proposed US using different cost function weightings for the C-spine (libCSpine) and TL-spine (libTLSpine) libraries. For libCSpine, prioritizing homogeneity (100% CV weighting) leads to a low CV (15%) but also a low efficiency (46%). Conversely, prioritizing efficiency (100% η weighting) results in a higher CV (32%) but also higher efficiency (90%). LibTLSpine exhibits a smaller range of achievable CV and η values. Prioritizing homogeneity (100% CV weighting) yields a CV of 16% and η of 74%, while

(A) Relative B_1^+ maps covering the C-spine


(B) Relative B_1^+ maps covering the TL-spine

FIGURE 2 This figure presents the relative channel-wise B_1^+ maps (magnitude and phase) for the first subject of group testCTLSpine, showcasing the channel distribution and B_1^+ homogeneity across the cervical spine (C-spine) and thoracic-lumbar spine (TL-spine) regions. (A) C-spine: The B_1^+ maps clearly demonstrate the U-shaped arrangement of channels positioned adjacent and posterior to the brain/neck region. (B) TL-spine: A representative 2D slice from the 3D B_1^+ maps of the TL-spine region is presented. Four channels are positioned on the chest, while four others are arranged under the subject's back. The phase angle of channels 2 to 8 are computed relative to channel 1.

prioritizing efficiency (100% η weighting) leads to a CV of 22% and η of 80%. The proposed weighting (5% CV, 95% η) achieves a balance between homogeneity and efficiency, resulting in a CV of 26% for libCSpine and 17% for libTLSpine, with a corresponding η of 82% and 78%, respectively. The different USs were calculated for a library size of six (libCSpine) and nine (libTLSpine) different subjects. The US performance for different library sizes in terms of CV and η have been computed in a retrospective simulation study and are shown in Figure S1. These simulations demonstrate that increasing the number of subjects in the library does not affect the robustness of the USs for B_1^+ field homogeneity and efficiency. For experimental validation, we focused only on the two proposed USs (US6 for cervical spine and US9 for thoracolumbar spine) and the two default RF shim configurations.

Figure 4 compares the default shim (not optimized for the C-spine) with a C-spine US. Qualitatively, the Figure shows the resulting B_1^+ transmit profiles and B_1^+ efficiency for all three subjects of libCSpine. While the default shim results in a variable and low B_1^+ transmit profile and efficiency $\eta(r)$, the C-spine US results in higher B_1^+ values and efficiency in the target region of subjects from libC-Spine and testCTLSpine. Quantitatively, the US showed a slight CV reduction (29% to 28%), and a two-fold increase in mean B_1^+ (11 to 20) and η (0.44 to 0.83) in the C-spine region (as outlined in the Figure by a white overlay).

Figure 5 compares the default shim (not optimized for the TL-spine) with a TL-spine US. B_1^+ predictions and RF efficiency are shown for all three subjects of libTLSpine along with a qualitative evaluation in the target regions outlined by a white overlay. Like the results shown in Figure 3 for the C-spine region, the results for the TL-spine region also show a variable and low B_1^+ transmit profile using the default RF shim setting. Both, the B_1^+ transmit homogeneity and efficiency are improved applying the US.
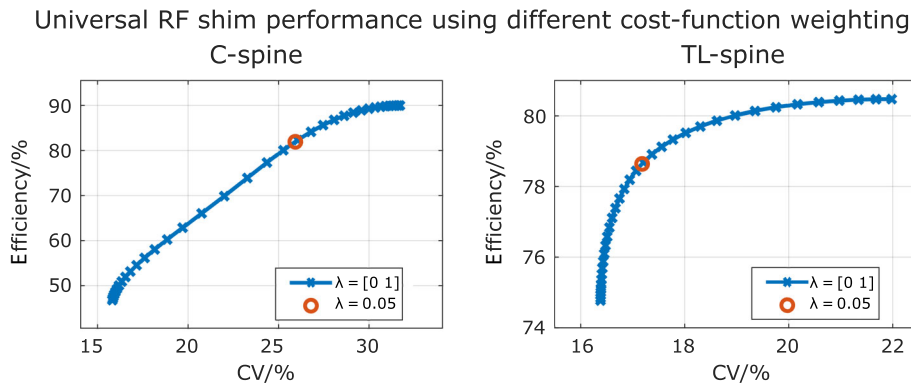
FIGURE 3 RF shim performance of different universal RF shims designed using different cost function weightings. Depicted are the B_1^+ transmit efficiency (η) and B_1^+ transmit homogeneity (measured by the CV) across all C-spine and TL-spine ROIs in libCSpine and libTLSpine, respectively. These two cost function terms are weighted by λ. For instance, $\lambda = 0$ indicates full weighting of η (100%) and no impact of the CV (0%). On the other hand, $\lambda = 1$ indicates full weighting of CV (100%) and no impact of the η (0%). The later used cost function weighting of 5% CV and 95% η is marked by a circle.

Quantitatively, the US reduced the CV two-fold (30% to 13%) and doubled η (0.42 to 0.78).

Figure 6 shows the absolute FA measurements utilizing the default RF shim and US for the C-spine and TL-spine of all subjects in the testCTLSpine group. The FA increase in the target regions (highlighted by a white overlay) is noticeable for the UP versus the default RF shim. Across all three subjects, measured FAs in the C-spine exhibited a 51% increase, from 52° (default) to 79° (US). Similarly, a 48% FA increase is observed in the TL-spine region, with average measured FAs of 25° (default) and 37° (US). Along the C-spine we observe a heterogeneous FA profile stemming from the cost function weighting (95% for η (efficiency) and 5% for CV (homogeneity)) which could be changed to homogeneity at the cost of B_1^+ transmit efficiency (see Figure 3).

Figure S4 depicts a representative slice of ΔB_0 maps obtained in the C-spine using a 2 mm isotropic dual-echo GRE sequence. Optimized shims yielded a significant decrease in RMS error (RMSE) (mean of 296 to 102 Hz) and SD (mean of 117 to 102 Hz) compared to vendor-supplied tune-up shims. Note that motion artifacts in the TL-spine region hindered tailored shimming in this area, necessitating further exploration of motion-robust approaches.

Figure 7 displays three orthogonal slices from a 3D multi-echo GRE dataset acquired during free-breathing using the proposed US in the C-spine and a tailored ΔB_0 shim for the first of three unseen test cases. A video showcasing the entire 3D volume for all unseen test cases is available in the Supporting Information Material. The image quality appears excellent in the C-spine and surrounding tissues, including the vertebrae, brainstem, and cerebellum, even though these areas were not explicitly considered in the pulse design.

Figures 8 and S4 showcase a sagittal slice of the 3D multi-echo GRE images obtained during free-breathing using US in the C-spine and a tailored ΔB_0 shim. Moreover, a 2D multi-echo GRE image was acquired during a breath-hold using US in the TL-spine for all three test subjects. Qualitatively, excellent image quality is apparent, even at longer TEs, as evident in Figure S5. This substantiates the feasibility of calibration-free pTx across the cervical, thoracic and lumbar SC.

4 | DISCUSSION

UHF SC MRI presents a unique set of challenges that hinder its widespread adoption in research and clinical settings[6]: First, the pronounced spatial magnetic field variations (ΔB_0) of several hundred Hz, second, the spatially variable FAs, signal voids, and spatially varying contrast induced by B_1^+ field inhomogeneities, and third, the large FAs that are often needed, particularly for sequences like MP2RAGE, FLAIR, and DTI, which demand high B_1^+ efficiency from the employed RF coil. Conventional combined-mode usage with static RF phase sets provided by coil manufacturers often restricts the coil's adaptability and limits its flexibility across different body regions. In our experience, coils optimized for other body regions, such as neck or cardiac region, exhibit dropout artifacts in the C-spine and TL-spine when utilized in the combined mode, rendering them unusable without pTx implementation. Even for dedicated C-spine RF coils, the performance based on vendor-provided shim settings may not be optimal, necessitating the use of tailored pTx to achieve the best possible coil performance.[33]

This study addresses the challenge of achieving uniform excitation across the C-spine and TL-spine

FIGURE 4 Prediction (A) and RF efficiency (B) in a single sagittal slice in the unseen test cases (testCTLSpine) utilizing the default shim setting and the optimized universal phase shim specifically designed for the six C-spine regions from the library. The US outperforms the default shim with lower CV (36% vs. 26%) and significantly increased RF efficiency (0.46 vs. 0.82) across the library and test cases, resulting in nearly a two-fold increase in the B_1^+ values, as demonstrated by the box plots in (A) when employing the US. Statistically significant outcomes are denoted by a star (*), while non-statistically significant results are indicated as "NS". The results in the library are shown in Figure S2.
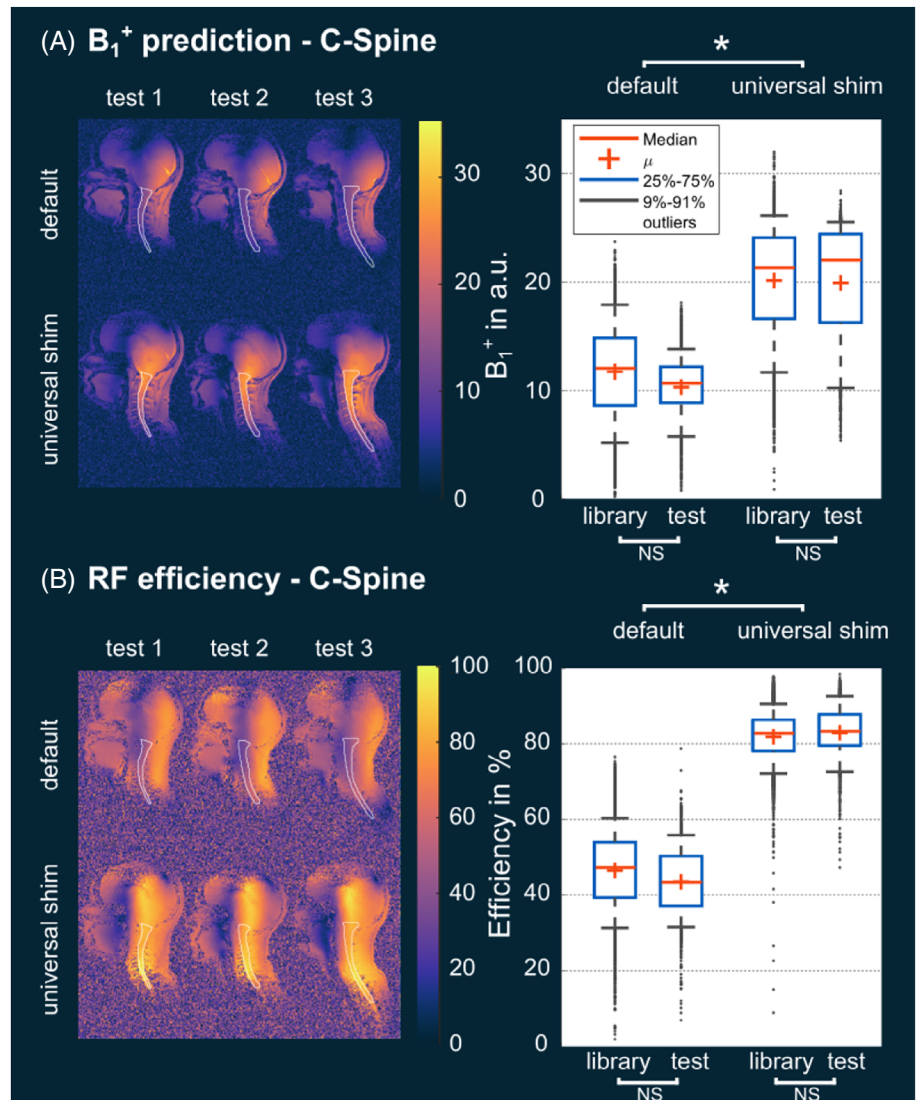
regions using pTx-enabled RF coils optimized for a different body region. Furthermore, the proposed utilization of calibration-free pTx alleviates the need for time-consuming calibration procedures associated with subject-specific tailored pTx. To address this, we have developed a pTx scheme based on a universal (phase-only) RF shim specifically designed for the C-spine and TL-spine regions, respectively. These US consistently demonstrate low CV values across unseen datasets and exhibit a significant two-fold enhancement in B_1^+ efficiency compared to the default shim setting, reaching approximately 0.8. This translates to the availability of approximately 80% of the coil's maximal RF B_1^+ magnitude, achieved with low CV values of 13% for the TL-spine and 28% for the C-spine region (the higher values being attributed to partial coil coverage of the lower C-spine elements).

We have observed a difference between the measured absolute FA increase of approximately 50% between default and US compared to the predicted two-fold

increase in B_1^+ efficiency based on the relative B_1^+ maps. This gap was consistent across both US experiments in the C-spine and the TL-spine, respectively. In this study, mapping of the relative 2D/3D magnetic field distribution for pTx pulse design was accomplished employing a small FA technique, rather than using absolute maps.[29,31,34] This approach was selected over alternative relative field mapping methods due to two primary advantages: its rapid acquisition time and its robustness against motion or flow artifacts stemming from short echo times. However, since the maps provide relative rather than absolute field values, they are subject to biases introduced by the square root of the proton density and the assumption that the sum of the magnitudes of all transmit channels is approximately equal to the sum of the magnitudes of all receive channels. Consequently, deviations from the actual field are anticipated, particularly in close proximity to the coil. Nonetheless, the same approach, which was employed here to attain B_1^+ maps, has been successfully applied in
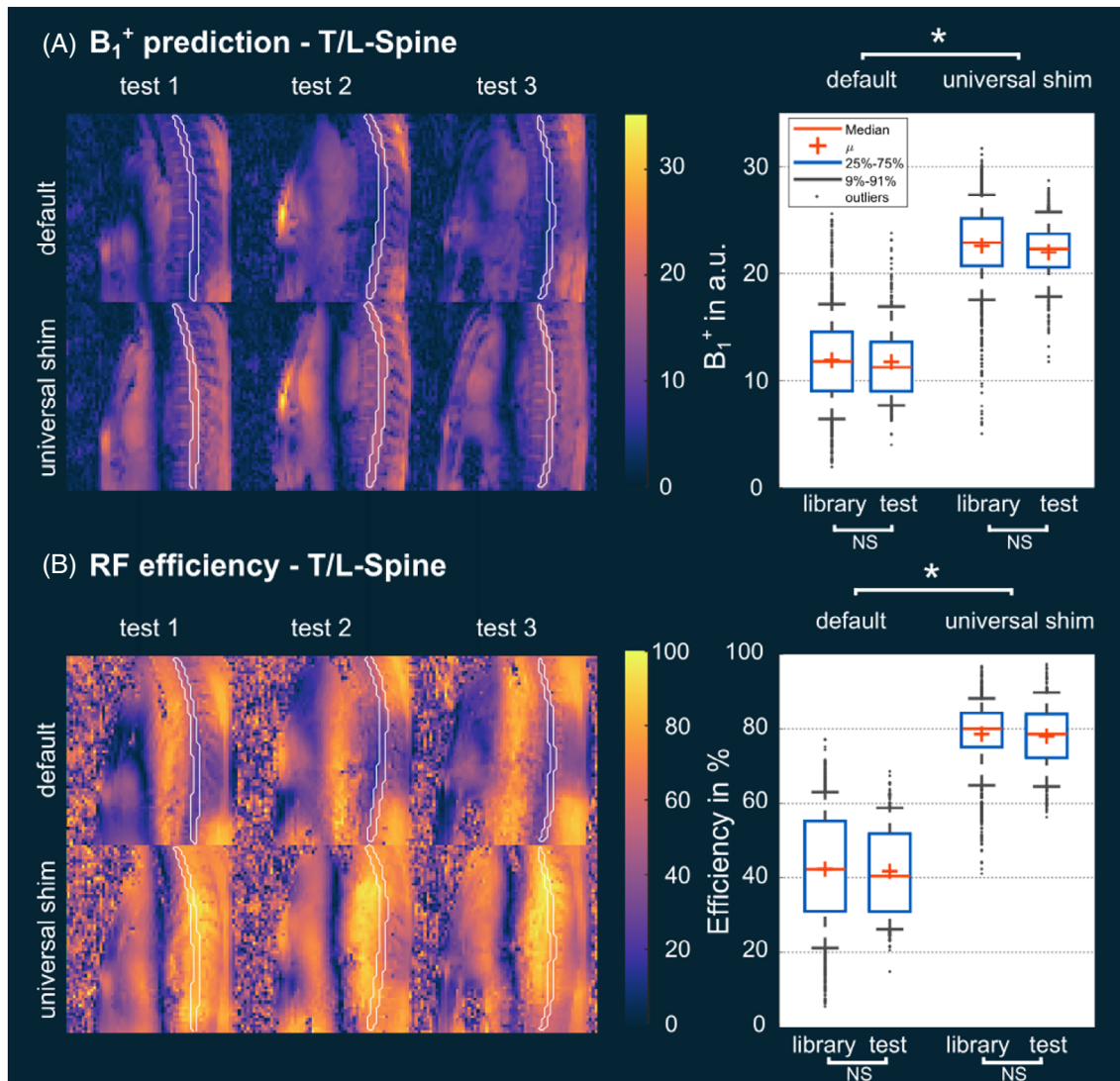
FIGURE 5 B_1^+ prediction (A) and RF efficiency (B) in a single sagittal slice in the unseen test cases utilizing the default shim setting and the optimized universal phase shim specifically designed for the nine TL-spine regions from the library. The US outperforms the default shim with lower CV (34% vs. 16%) and significantly increased RF efficiency (0.42 vs. 0.78) across the library and test cases, resulting in nearly a two-fold increase in the B_1^+ values, as demonstrated by the box plots in (A) when employing the US. Statistically significant outcomes are denoted by a star (*), while non-statistically significant results are indicated as "NS". The results in the library are shown in Figure S3.

several applications in the human body at 7T, including the generation of shimming solutions, spokes pTx pulses and non-selective kT-points pTx pulses for the heart.[19,20,27,31,35] However, the aforementioned assumptions in the relative B_1^+ mapping might explain the differences between the measured absolute FA increase of approximately 50%. Another contributing factor might be deviations resulting from the employed absolute mapping method[32] that is known to suffer from limited accuracy and dynamic range in regions with low SNR. If higher accuracy is needed, hybrid B_1^+ mapping method based on MR fingerprinting[36] or more advanced turbo flash approaches[33] could be considered. The proposed US scheme offers comparable B_1^+ performance to tailored RF shimming while eliminating

the need for extensive calibration times, typically ranging from 5 to 10 min.

The relatively long calibration time of up to 10 min arises from the implementation of our custom B_1^+ adjustment framework, encompassing B_1^+ mapping (1–4 min), raw data export (<1 min), B_1^+ map reconstruction and computation (~1 min), manual ROI placement (~1 min), tailored RF shimming and quality checks (~1 min), and pulse file generation and export to the MR scanner (~1 min). While the vendors could partially streamline this workflow by incorporating these steps directly into the MR console of their latest generation 7T scanners, tailored pTx still demands a significant time investment of several minutes. The proposed US in the C-spine and TL-spine, respectively,
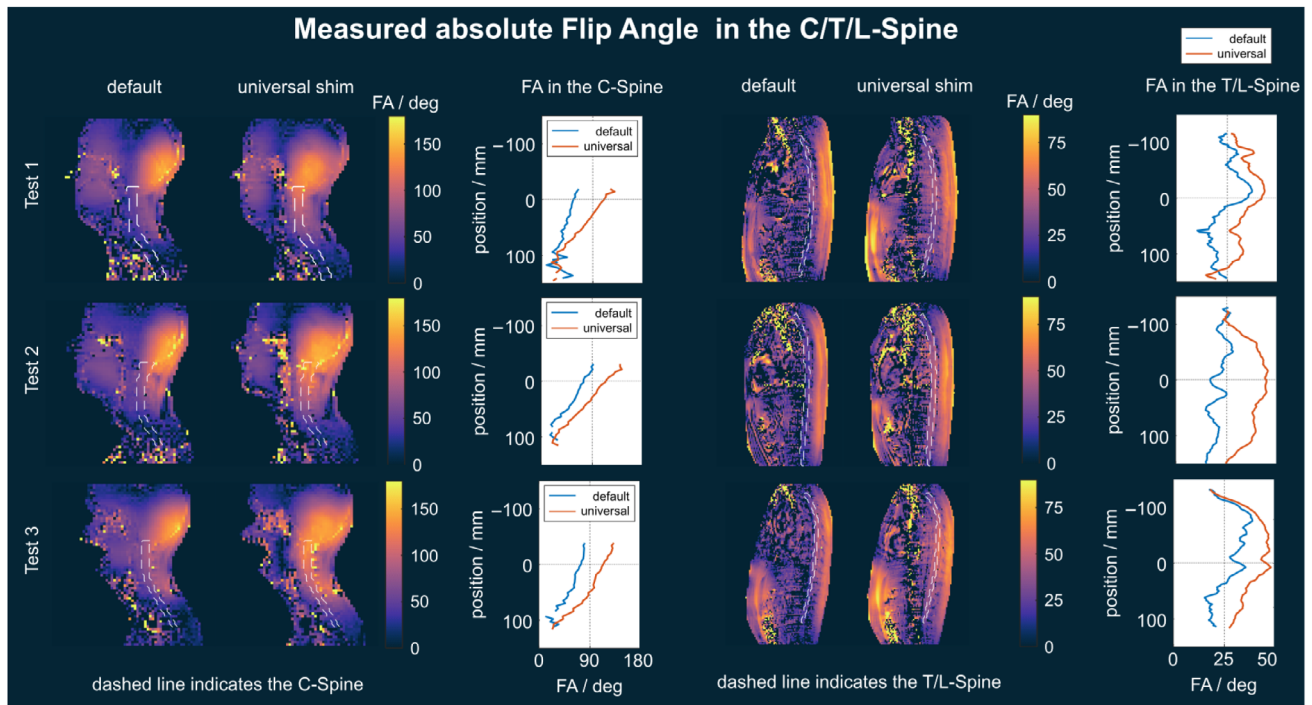
FIGURE 6 Measured FAs in a single sagittal 2D-slice employing a TFL approach in the C-spine and TL-spine of the three test cases (target FA of 90°). In both regions, two sets of FA measurements are presented: the first utilizing the default shim, and the second employing the US optimized for the respective libraries. The line plot illustrating the mean flip angles (FAs) along the SC reveals significantly elevated FAs (approximately a 50% increase in both regions) when the US is applied. To effectively suppress noise outside the body, the measured B_1^+ maps were subjected to manual masking based on a sum-of-squares image derived from the 8/32 receive channels of the two employed RF coils.

FIGURE 7 3D view of the multi-echo GRE data in the C-spine using the calibration-free universal RF shim in the first of the three unseen test cases. The data were acquired during free breathing in 3D with a 1 mm isotropic resolution.
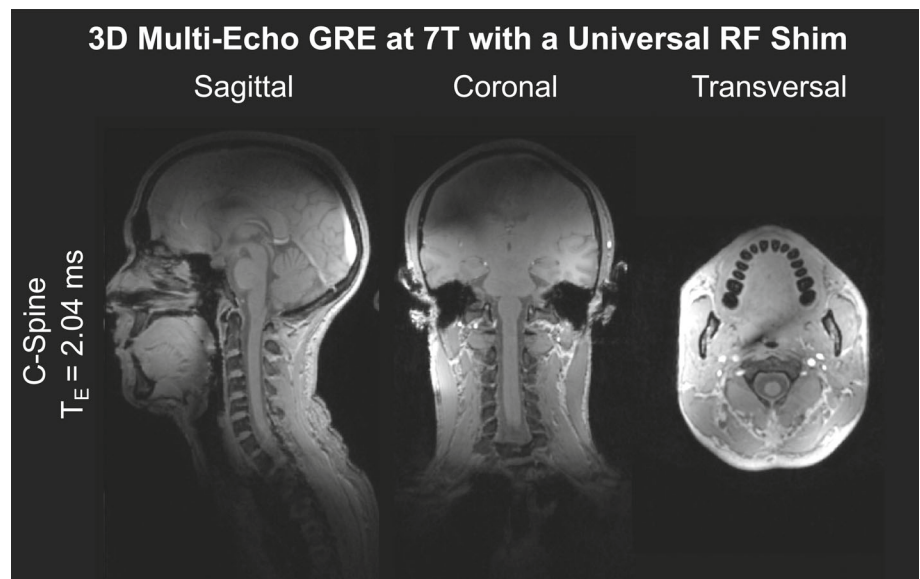
offer the flexibility to be implemented as a "combined mode" hardware solution with tailored local SAR supervision adjustments, particularly in terms of power per channel limit values.

Additionally, several studies have highlighted the detrimental impact of motion on the efficacy of tailored RF shims and dynamic RF pulses.[37,38] This effect stems from potential discrepancies between the acquired B_1^+ maps and the actual B_1^+ transmit profiles during RF pulse application due to patient motion, respiration, or other displacements. In contrast, several studies demonstrated an inherent motion robustness of universal pulses due to anatomical
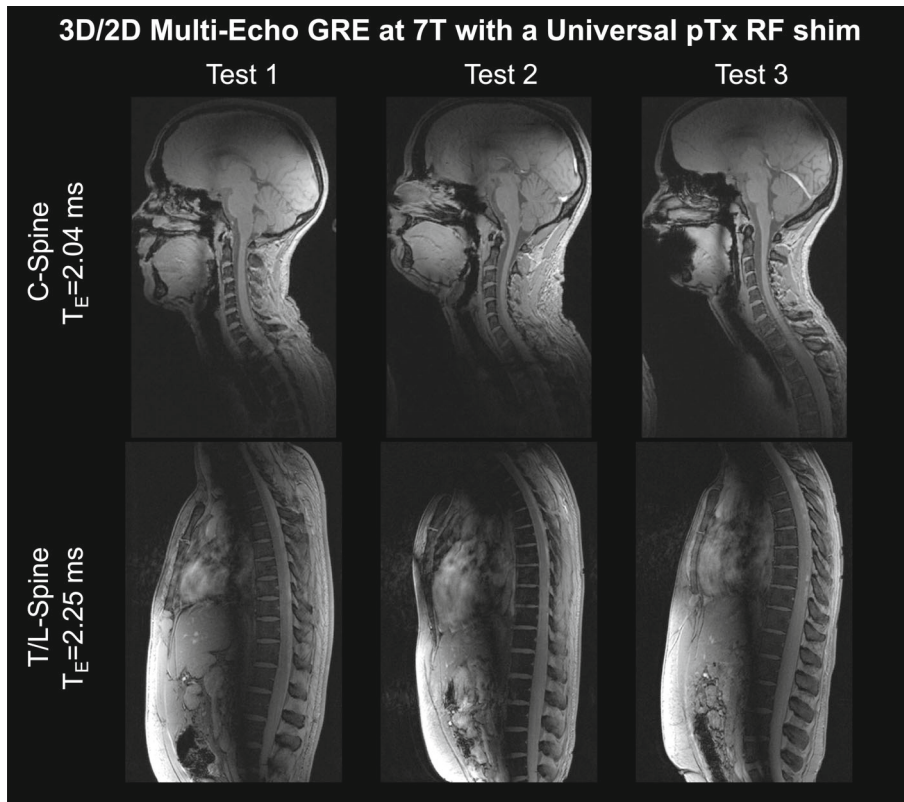
FIGURE 8 2D and 3D multi-echo GRE data in the C-spine and TL-spine. The TL-spine data presents a single 2D slice acquired during a breath-hold (1 mm in-plane resolution; 2 mm slice thickness), while the C-spine is imaged during free-breathing in 3D with a 1 mm isotropic resolution. Data from a later echo time are shown in Figure S5.

intersubject differences and resulting spatial differences of the underlying B_1^+ maps and target regions.[19,20]

Calibration-free pTx employing universal RF pulses effectively alleviates the challenges associated with lengthy and error-prone tailored pTx approaches and has been successfully implemented in various body regions, including the brain, heart, and C-spine.[16,19,21,25] However, only a few studies have explored the use of universal RF shims for specific applications, such as localized spectroscopy[17] or a simulation study that focused on combined brain-neck imaging,[18] with the latter work limited to simulations, despite their inherent advantages in terms of ease of design and application. Moreover, this shortage of applications is striking given that the temporal B_1^+ efficiency of dynamic pulses, such as kT-point pulses, is compromised by the additional RF dead time during gradient blips. Additionally, dynamic pulses necessitate external loading into the sequences, often requiring modifications to the sequence source code and custom compilation. While dynamic pTx offers greater degrees of freedom compared to RF shimming, particularly useful for pTx of larger volumes encompassing the entire brain, liver, or heart, our results demonstrate that RF shimming with the employed coils is sufficient for the long, but relatively narrow diameter of the SC. In this work, we prioritize achieving high B_1^+ efficiency, as opposed to solely maximizing spatial B_1^+ homogeneity, which has been shown to negatively impact B_1^+ efficiency.[15] This was achieved by optimizing the cost function with a weighting of 95% for B_1^+ efficiency and 5% for B_1^+ homogeneity measured by the CV. This ratio can be tailored to accommodate specific requirements, such as enhancing B_1^+ homogeneity at the expense of RF performance with more efficient RF coils.

We have also investigated the potential benefits of designing universal magnitude and phase RF shims compared to the proposed phase-only US. While simulations showed improvements in terms of transmit homogeneity or efficiency (e.g., C-spine magnitude and phase US resulted in a CV reduction from 26% to 19% with fixed transmit efficiency compared to a phase-only US), practical limitations emerged. The optimized magnitude solutions often had extreme values (e.g., the above-mentioned C-Spine magnitude and phase US solution had four channels with a magnitude close to 0 and four channels with a magnitude close to 2). In our pTx setting, RF power constraints are enforced per channel to meet local SAR limitations. Using such a magnitude distribution with unequal RF power allocation would lead to lower overall RF performance compared to the phase-only case (e.g., lower achievable FAs before reaching SAR limits).

This study investigated the feasibility and advantages of employing calibration-free pTx via US to facilitate and expedite SC imaging at 7T. The results demonstrate that US markedly enhances the B_1^+ efficiency and B_1^+ uniformity within the targeted C-spine and TL-spine regions, with minimal loss of performance compared to tailored

shimming. Moreover, the application of calibration-free pTx-based US extends the imaging capabilities of the employed coils, enabling the simultaneous acquisition of both the C-spine and cerebellum, or the vertebrae, intervertebral discs, and the SC itself. This expansion of imaging scope paves the way for more comprehensive SC investigations at UHF. Furthermore, the calibration-free nature of pTx-based US eliminates the need for extensive pTx expertise and prolonged adjustment time, significantly streamlining the imaging workflow. These findings underscore the transformative potential of calibration-free pTx in pushing SC imaging at UHF and beyond.

5 | CONCLUSIONS

This in-vivo study demonstrates the experimental implementation and highlights the advantages of universal RF shims for calibration-free SC imaging at 7T for different SC regions and RF coils. The proposed US approach achieved very high B_1^+ efficiency of approximately 80% of the theoretical coil maximum. The application of US enables seamless pTx in the SC, eliminating the requirement for time-consuming calibration procedures. This approach, in combination with motion-robust non-Cartesian approaches, holds promise for advancing SC imaging capabilities at UHF.

AFFILIATIONS

[1]Physikalisch-Technische Bundesanstalt (PTB), Braunschweig and Berlin, Germany

[2]Working Group on Cardiovascular Magnetic Resonance, Experimental and Clinical Research Center, A Joint Cooperation between the Charité Medical Faculty and the Max-Delbrück Center for Molecular Medicine, Berlin, Germany

[3]NeuroPoly Lab, Institute of Biomedical Engineering, Polytechnique Montréal, Montréal, Quebec, Canada

[4]Centre de recherche du CHU Sainte-Justine, Université de Montréal, Montréal, Quebec, Canada

[5]Functional Neuroimaging Unit, CRIUGM, Université de Montréal, Montréal, Quebec, Canada

[6]Mila-Quebec AI Institute, Montréal, Quebec, Canada

[7]Medical Physics in Radiology, German Cancer Research Center (DKFZ), Heidelberg, Germany

[8]Center for Magnetic Resonance Research, University of Minnesota, Minneapolis, Minnesota, USA

DATA AVAILABILITY STATEMENT
The source code, the used parameters, and the relative B_1^+ datasets can be found at: https://github.com/chaigner/UShim.

ORCID
Christoph S. Aigner https://orcid.org/0000-0003-3618-9610

Eva Alonso-Ortiz https://orcid.org/0000-0001-6590-7234

Julien Cohen-Adad https://orcid.org/0000-0003-3662-9532

Sebastian Schmitter https://orcid.org/0000-0003-4410-6790

REFERENCES
1. Ladd ME, Bachert P, Meyerspeer M, et al. Pros and cons of ultra-high-field MRI/MRS for human application. *Prog Nucl Magn Reson Spectrosc*. 2018;109:1-50. doi:10.1016/j.pnmrs.2018.06.001

2. Kreiter DJ, van den Hurk J, Wiggins CJ, Hupperts RMM, Gerlach OHH. Ultra-high field spinal cord MRI in multiple sclerosis: where are we standing? A literature review. *Mult Scler Relat Disord*. 2022;57:103436. doi:10.1016/j.msard.2021.103436

3. Straub S, El-Sanosy E, Emmerich J, Sandig FL, Ladd ME, Schlemmer H. Quantitative magnetic resonance imaging biomarkers for cortical pathology in multiple sclerosis at 7 T. *NMR Biomed*. 2023;36:e4847. doi:10.1002/nbm.4847

4. El Mendili MM, Querin G, Bede P, Pradat PF. Spinal cord imaging in amyotrophic lateral sclerosis: historical concepts—novel techniques. *Front Neurol*. 2019;10:350. doi:10.3389/fneur.2019.00350

5. Bruschi N, Boffa G, Inglese M. Ultra-high-field 7-T MRI in multiple sclerosis and other demyelinating diseases: from pathology to clinical practice. *Eur Radiol Exp*. 2020;4:59. doi:10.1186/s41747-020-00186-x

6. Barry RL, Vannesjo SJ, By S, Gore JC, Smith SA. Spinal cord MRI at 7T. *Neuroimage*. 2018;168:437-451. doi:10.1016/j.neuroimage.2017.07.003

7. Massire A, Feiweier T, Kober T, et al. MR imaging of the cervical spinal cord at 7T: a multiparametric portfolio. *MAGNETOM Flash*. 2018;70:112-119.

8. Zhao W, Cohen-Adad J, Polimeni JR, et al. Nineteen-channel receive array and four-channel transmit array coil for cervical spinal cord imaging at 7T: RF Coil for Spinal Cord MRI at 7T. *Magn Reson Med*. 2014;72:291-300. doi:10.1002/mrm.24911

9. Conrad BN, Barry RL, Rogers BP, et al. Multiple sclerosis lesions affect intrinsic functional connectivity of the spinal cord. *Brain*. 2018;141:1650-1664. doi:10.1093/brain/awy083

10. Massire A, Rasoanandrianina H, Taso M, et al. Feasibility of single-shot multi-level multi-angle diffusion tensor imaging of the human cervical spinal cord at 7T: transverse 7T DTI of the Whole Cervical Spinal Cord. *Magn Reson Med*. 2018;80:947-957. doi:10.1002/mrm.27087

11. Dula AN, Pawate S, Dethrage LM, et al. Chemical exchange saturation transfer of the cervical spinal cord at 7 T: Cest of the Cervical Spinal Cord AT 7 T. *NMR Biomed*. 2016;29:1249-1257. doi:10.1002/nbm.3581

12. Geldschläger O, Bosch D, Avdievich NI, Henning A. Ultrahigh-resolution quantitative spinal cord MRI at 9.4T. *Magn Reson Med*. 2021;85:1013-1027. doi:10.1002/mrm.28455

13. Vaughan JT, Snyder CJ, DelaBarre LJ, et al. Whole-body imaging at 7T: preliminary results: 7T body MRI. *Magn Reson Med*. 2009;61:244-248. doi:10.1002/mrm.21751

14. Kraff O, Bitz AK, Kruszona S, et al. An eight-channel phased array RF coil for spine MR imaging at 7 T. *Invest Radiol*. 2009;44:734-740. doi:10.1097/RLI.0b013e3181b24ab7

15. Padormo F, Beqiri A, Hajnal JV, Malik SJ. Parallel transmission for ultrahigh-field imaging: parallel transmission for ultrahigh-field imaging. *NMR Biomed*. 2016;29:1145-1161. doi:10.1002/nbm.3313

16. Gras V, Vignaud A, Amadon A, Bihan D, Boulant N. Universal pulses: a new concept for calibration-free parallel transmission. *Magn Reson Med*. 2017;77:635-643. doi:10.1002/mrm.26148

17. Berrington A, Považan M, Mirfin C, et al. Calibration-free regional RF shims for MRS. *Magn Reson Med*. 2021;86:611-624. doi:10.1002/mrm.28749

18. Kazemivalipour E, May MW, Rangaprakash D, et al. Design of a universal RF-shimming drive mode for head and neck imaging at 7 tesla using a 16-channel pTx array. In: *Proceedings Annual Meeting ISMRM*, 2023:4406.

19. Aigner CS, Dietrich S, Schaeffter T, Schmitter S. Calibration-free pTx of the human heart at 7T via 3D universal pulses. *Magn Reson Med*. 2022;87:70-84. doi:10.1002/mrm.28952

20. Aigner CS, Dietrich S, Schmitter S. Respiration induced B_1^+ changes and their impact on universal and tailored 3D kT-point parallel transmission pulses for 7T cardiac imaging. *Magn Reson Med*. 2022;87:2862-2871. doi:10.1002/mrm.29183

21. Papp D, Boulant N, Massire A, Mauconduit F, Gras V, Cohen-Adad J. Universal pulses for the cervical spinal cord at 7T: a feasibility study. In: *Proceedings Annual Meeting ISMRM*, 2023:199.

22. Ianni JD, Cao Z, Grissom WA. Machine learning RF shimming: prediction by iteratively projected ridge regression. *Magn Reson Med*. 2018;80:1871-1881. doi:10.1002/mrm.27192

23. Tomi-Tricot R, Gras V, Mauconduit F, et al. B_1 artifact reduction in abdominal DCE-MRI using k_T-points: first clinical assessment of dynamic RF shimming at 3T. *J Magn Reson Imaging*. 2018;47:1562-1571. doi:10.1002/jmri.25908

24. Herrler J, Liebig P, Gumbrecht R, et al. Fast online-customized (FOCUS) parallel transmission pulses: a combination of universal pulses and individual optimization. *Magn Reson Med*. 2021;85:3140-3153. doi:10.1002/mrm.28643

25. Le Ster C, Mauconduit F, Massire A, Boulant N, Gras V. Standardized universal pulse: a fast RF calibration approach to improve flip angle accuracy in parallel transmission. *Magn Reson Med*. 2022;87:2839-2850. doi:10.1002/mrm.29180

26. Aigner CS, Dietrich-Conzelmann S, Lutz M, Krüger F, Schmitter S. Tailored and universal parallel transmit broadband pulses for homogeneous 3D excitation of the human heart at 7T. *Magn Reson Med*. 2022:1-11. doi:10.1002/mrm.30072

27. Aigner CS, Dietrich S, Schmitter S. Three-dimensional static and dynamic parallel transmission of the human heart at 7 T. *NMR Biomed*. 2021;34:e4450. doi:10.1002/nbm.4450

28. D'Astous A, Cereza G, Papp D, et al. Shimming toolbox: an open-source software toolbox for B_0 and B1 shimming in MRI. *Magn Reson Med*. 2023;89:1401-1417. doi:10.1002/mrm.29528

29. Dietrich S, Aigner CS, Kolbitsch C, et al. 3D free-breathing multichannel absolute mapping in the human body at 7T. *Magn Reson Med*. 2021;85:2552-2567. doi:10.1002/mrm.28602

30. De Leener B, Lévy S, Dupont SM, et al. SCT: Spinal Cord Toolbox, an open-source software for processing spinal cord MRI data. *Neuroimage*. 2017;145:24-43. doi:10.1016/j.neuroimage.2016.10.009

31. Schmitter S, DelaBarre L, Wu X, et al. Cardiac imaging at 7 tesla: single- and two-spoke radiofrequency pulse design with 16-channel parallel excitation: cardiac imaging at 7T. *Magn Reson Med*. 2013;70:1210-1219. doi:10.1002/mrm.24935

32. Fautz HP, Vogel M, Gross P, Kerr A, Zhu Y. B_1 mapping of coil arrays for parallel transmission. *Proc 16th Annu Meet ISMRM*. 2008;16:1247.

33. Destruel A, Mauconduit F, Massire A, et al. Optimized interferometric encoding of presaturated TurboFLASH B_1 mapping for parallel transmission MRI at 7 T: preliminary application for quantitative T_1 mapping in the spinal cord. *Magn Reson Med*. 2023;90:1328-1344. doi:10.1002/mrm.29708

34. Van De Moortele PF, Ugurbil K. Very fast multi channel B_1 calibration at high field in the small flip angle regime. *Proc Intl Soc Mag Reson Med*. 2009;17:367.

35. Dietrich S, Aigner CS, Mayer J, et al. Motion-compensated fat-water imaging for 3D cardiac MRI at ultra-high fields. *Magn Reson Med*. 2022;87:2621-2636. doi:10.1002/mrm.29144

36. Lutz M, Aigner CS, Dietrich S, et al. Low power free-breathing absolute B_1^+ mapping in the human body at 7T using magnetic resonance fingerprinting. In: *Proceedings Annual Meeting ISMRM*, 2022. 386.

37. Schön N, Petzold J, Seifert F, Aigner CS, Metzger G. Impact of respiration on B_1^+ field and SAR distribution at 7 T using a novel EM simulation setup. In: *Proceedings Annual Meeting ISMRM*, 2020:1120.

38. Plumley A, Watkins L, Treder M, Liebig P, Murphy K, Kopanoglu E. Rigid motion-resolved prediction using deep learning for real-time parallel-transmission pulse design. *Magn Reson Med*. 2022;87:2254-2270. doi:10.1002/mrm.29132

SUPPORTING INFORMATION

Additional supporting information may be found in the online version of the article at the publisher's website.

FIGURE S1. Retrospective simulation study that shows the impact of different library sizes on the RF shim performance in terms of B_1^+ transmit homogeneity measured by the Coefficient of Variation (CV) and the B_1^+ transmit

efficiency (η). The subscript indicates how many different subjects were included in the pulse design. All RF shims were evaluated on all subjects (9 for the C-spine and 12 for the TL-spine). In the experimental validation, we measured the absolute B_1^+ maps with the two proposed universal shims (US6 for the C-spine and US9 for the TL-spine) and the two default RF shim configurations.

Figure S2. Prediction (A) and RF efficiency (B) in a single sagittal slice utilizing the default shim setting and the optimized universal phase shim specifically designed for the six C-spine regions from the library. The Universal Shim (US) outperforms the default shim with lower coefficient of variation (CV) (36% vs. 26%) and significantly increased RF efficiency (0.46 vs. 0.82) across the library and test cases, resulting in nearly a two-fold increase in the B_1^+ values.

Figure S3. B_1^+ prediction (A) and RF efficiency (B) in a single sagittal slice utilizing the default shim setting and the optimized universal phase shim specifically designed for the nine TL-spine regions from the library. The Universal Shim (US) outperforms the default shim with lower coefficient of variation (CV) (34% vs. 16%) and significantly increased RF efficiency (0.42 vs. 0.78) across the library and test cases, resulting in nearly a two-fold increase in the B_1^+ values.

Figure S4. Measured GRE-based field map of a single sagittal slice, selected from a 3D volume, utilizing the Universal Shim setting in the C-spine of the three test cases, both before and after 2nd order B_0 shimming to address magnetic field inhomogeneities within the spinal cord.

The shim volume is outlined with a dashed line and was performed for the entire 3D SC volume using the SC Shimming Toolbox. The unshimmed and shimmed field maps unveil persistent high-frequency field distortions along the cord, particularly near the intervertebral junctions.

Figure S5. 2D and 3D multi-echo GRE data in the C-spine and TL-spine at a later echo time compared to the data shown in Figure 7. The TL-spine data presents a single 2D slice acquired during a breath-hold (1 mm in-plane resolution; 2 mm slice thickness), while the C-spine is imaged during free-breathing in 3D with a 1 mm isotropic resolution.

Video S1. "Animation of sagittal images at the first echo time from a 3D multi-echo GRE acquisition of the cervical spine using the proposed calibration-free universal RF shim in all three test cases. The data was acquired at 1 mm isotropic resolution during free breathing. To comply with local data security rules, the area around the eyes has been masked. More image data for other orientations and later echo times can be found in Figures 7 and 8 and Supporting Information Figure S5."